A&A, 682, A116 (2024)
https://doi.org/10.1051/0004-6361/202348392

Astronomy & Astrophysics

Abundances of iron-peak elements in accreted and in situ born Galactic halo stars⋆,⋆⋆

P. E. Nissen[1], A. M. Amarsi[2], Á. Skúladóttir[3,4], and W. J. Schuster[5]

[1] Department of Physics and Astronomy, Aarhus University, Ny Munkegade 120, 8000 Aarhus C, Denmark
e-mail: pen@phys.au.dk
[2] Theoretical Astrophysics, Department of Physics and Astronomy, Uppsala University, Box 516, 751 20 Uppsala, Sweden
[3] Dipartimento di Fisica e Astronomia, Università degli Studi di Firenze, Via G. Sansone 1, 50019 Sesto Fiorentino, Italy
[4] INAF/Osservatorio Astrofisico di Arcetri, Largo E. Fermi 5, 50125 Firenze, Italy
[5] Instituto de Astronomia, Universidad Nacional Autónoma de México, AP 106, Ensenada 22800, BC, Mexico

Received 26 October 2023 / Accepted 4 December 2023

ABSTRACT

Context. Studies of the element abundances and kinematics of stars belonging to the Galactic halo have revealed the existence of two distinct populations: accreted stars with a low [α/Fe] ratio and in situ born stars with a higher ratio.
Aims. Previous work on the abundances of C, O, Na, Mg, Si, Ca, Ti, Cr, Mn, Fe, Ni, Cu, and Zn in high-α and low-α halo stars is extended to include the abundances of Sc, V, and Co, enabling us to study the nucleosynthesis of all iron-peak elements along with the lighter elements.
Methods. The Sc, V, and Co abundances were determined from a 1D MARCS model-atmosphere analysis of equivalent widths of atomic lines in high signal-to-noise, high resolution spectra assuming local thermodynamic equilibrium (LTE). In addition, new 3D and/or non-LTE calculations were used to correct the 1D LTE abundances for several elements including consistent 3D non-LTE calculations for Mg.
Results. The two populations of accreted and in situ born stars are well separated in diagrams showing [Sc/Fe], [V/Fe], and [Co/Fe] as a function of [Fe/H] . The [X/Mg] versus [Mg/H] trends for high-α and low-α stars were used to determine the yields of core-collapse and Type Ia supernovae. The largest Type Ia contribution occurs for Cr, Mn, and Fe, whereas Cu is a pure core-collapse element. Sc, Ti, V, Co, Ni, and Zn represent intermediate cases. A comparison with yields calculated for supernova models shows poor agreement for the core-collapse yields. The Ia yields suggest that sub-Chandrasekhar-mass Type Ia supernovae provide a dominant contribution to the chemical evolution of the host galaxies of the low-α stars. A substructure in the abundances and kinematics of the low-α stars suggests that they arise from at least two different satellite accretion events, Gaia-Sausage-Enceladus and Thamnos.

Key words. stars: abundances – stars: atmospheres – supernovae: general – Galaxy: formation – Galaxy: halo

1. Introduction

In a study of the chemical composition of high-velocity stars, Nissen & Schuster (2010; 2011, hereafter Papers I and II) found that F and G dwarf stars with halo kinematics split into two distinct populations: (i) one with a high ratio between the abundance of α-capture elements and iron ([α/Fe] $\simeq$ 0.3)[1] similar to stars with thick-disk kinematics; and (ii) a population with [α/Fe] decreasing from ∼0.3 dex at a metallicity of [Fe/H] = −1.6 to [α/Fe] $\simeq$ 0.1 at [Fe/H] = −0.8. A clear separation between the two populations was also found for [Na/Fe], [Ni/Fe], [Cu/Fe], and [Zn/Fe], whereas [Cr/Fe] and [Mn/Fe] overlap in their metallicity trends. In a third paper (Schuster et al. 2012), the space velocities of the stars were used to show that the low-α stars move on radial orbits with maximum Galactocentric distances r_{max} up to 30–40 kpc, whereas the high-alpha stars move on more circular orbits with r_{max} up to about 16 kpc. Furthermore, it was found that the low-α stars tend to be 2–3 Gyr younger than the high-α halo stars. All of this was interpreted in a scenario in which the high-α stars were formed in situ during the fast collapse of the proto-Galactic gas cloud with only core-collapse supernovae (CC SNe) contributing to the chemical enrichment, whereas the low-α stars were accreted from dwarf galaxies with a slower star formation rate allowing Type Ia supernovae (Ia SNe) to contribute to the chemical evolution.

The existence of two discrete halo populations is supported by carbon and oxygen abundances derived by Amarsi et al. (2019) from a 3D model-atmosphere analysis of equivalent widths of C I, O I, and Fe II lines taking departures from local thermodynamic equilibrium (LTE) into account. The dichotomy in halo star abundances is also confirmed in the analysis of abundance data from the Apache Point Observatory Galactic Evolution Experiment (APOGEE) for large samples of K giants by Hawkins et al. (2015) and Hayes et al. (2018), who added [Al/Fe] and [Al/Mn] as very useful indicators of the separation between accreted and in situ born stars. We note that aluminium was not included in Papers I and II, because there are no suitable Al lines available in the spectra used for the investigation.

⋆ Table A.1 is available at the CDS via anonymous ftp to cdsarc.cds.unistra.fr (130.79.128.5) or via https://cdsarc.cds.unistra.fr/viz-bin/cat/J/A+A/682/A116

⋆⋆ Based on data products from observations made with ESO Telescopes at the La Silla Paranal Observatory and the Nordic Optical Telescope under programmes given in Tables 1 and 2 of Paper I.

[1] For two elements, X and Y, with number densities N_X and N_Y, [X/Y] $\equiv \log(N_X/N_Y)_{star} - \log(N_X/N_Y)_{\odot}$ and [α/Fe] is an unweighted mean of [Mg/Fe], [Si/Fe], [Ca/Fe], and [Ti/Fe].

With the advent of *Gaia* data, it was realised that halo stars in the solar neighbourhood show an orbital anisotropy in the radial direction and an elongated structure in the Toomre velocity diagram (Belokurov et al. 2018; Helmi et al. 2018). This has been interpreted as a signature of a merger of the Milky Way with a massive dwarf galaxy named Gaia-Sausage-Enceladus (GSE) in which the majority of the low-α stars were born (Helmi 2020), but other merging dwarf galaxies have probably also contributed to the low-α population causing a cosmic scatter in [α/Fe], [Na/Fe], and [Ni/Fe] at a given [Fe/H] (e.g. Myeong et al. 2019; Matsuno et al. 2022a,b; Horta et al. 2023; Donlon & Newberg 2023). The high-α stars have been explained as being born in a precursor to the Galactic thick disk and dynamically heated to halo kinematics due to the GSE merger, the so-called big splash (Belokurov et al. 2020), although the more metal-poor part of the high-α population may consist of stars born in situ from infalling gas before the formation of a disk (Belokurov & Kravtsov 2022; Myeong et al. 2022; Feltzing & Feuillet 2023).

In the last decade, there have also been several interesting studies of the relative ages of high-α and low-α stars. Ge et al. (2016) found the same age difference of about 2 Gyr as Schuster et al. (2012) when using stellar models with C and O abundances from Nissen et al. (2014). A much larger sample of about 15 000 stars in the turn-off region was analysed by Hawkins et al. (2014), who used Sloan Digital Sky Survey low-resolution spectra to derive a spectral index of [α/Fe]. From a comparison with isochrones, they found an age difference of about 1 Gyr between high-α and low-α stars in the metallicity range $-1.2 <$ [Fe/H] < -0.9 but an equal age of the two populations for more metal-poor stars. A similar metallicity trend of the age difference between in situ and accreted globular clusters was found by Massari et al. (2019). Furthermore, Xiang & Rix (2022) used precise age determinations of 150 000 subgiant stars, based on estimates of effective temperature $T_{\rm eff}$, absolute magnitude M_K, [Fe/H], and [α/Fe] from the Large Sky Area Multi-Object fiber Spectroscopic Telescope (LAMOST) survey (Zhao et al. 2012), to show that high-α halo stars are 1–2 Gyr older than low-α stars at a metallicity of [Fe/H] ~ -1.0. These results support the idea that the star formation rate in the host galaxies of the low-α stars has been so slow that Ia SNe have significantly contributed to the chemical evolution at low [Fe/H] (e.g. Fernández-Alvar et al. 2018; Vincenzo et al. 2019), whereas the high-α stars are more likely to have been born from gas that is enriched by only CC SNe. A particularly interesting modelling of the evolution of abundance ratios in the GSE dwarf galaxy has been published by Sanders et al. (2021); from the metallicity trends of [Mn/Fe] and [Ni/Fe], they find that sub-Chandrasekhar-mass (sub-$M_{\rm Ch}$) Ia SNe provide a significant contribution to the chemical evolution.

With these recent results in mind, we decided to have a fresh look at the abundances for the high-α and low-α populations in Papers I and II and to add abundances of Sc, V, and Co. Thus, we can provide the most precise and accurate iron-peak abundances available for in situ and ex situ halo stars, allowing important tests of star formation and nucleosynthesis.

2. Sc, V, and Co abundances

In Papers I and II, abundances of Na, Mg, Si, Ca, Ti, Cr, Mn, Fe, Ni, Cu, and Zn were determined for 94 main-sequence stars selected from Strömgren photometry (Schuster et al. 2006) to have metallicities in the range $-1.6 <$ [Fe/H] < -0.4 and $T_{\rm eff}$ from 5300 K to 6400 K. Fishlock et al. (2017) have determined Sc abundances for 27 of these stars, but using only the Sc II line at 5526.8 Å. We have used eight Sc II lines (see Table 1) and derived Sc abundances for 85 stars, that is, those included in the papers on C and O abundances by Nissen et al. (2014) and Amarsi et al. (2019). In addition, V and Co abundances were determined from a set of four lines for each element as listed in Table 1. These lines are too weak to be measured for the warmer and more metal-poor stars in our sample, but we were able to derive reliable V and Co abundances for 60 and 59 stars, respectively.

Table 1. Spectral line data and equivalent widths.

ID	Wavelength (Å)	$\chi_{\rm exc}$ (eV)	log(gf) [(a)]	EW [(b)] (mÅ)	EW [(c)] (mÅ)	Ref. HFS
ScII	5239.82	1.46	−0.75	29.7	31.5	1
ScII	5526.82	1.77	−0.05	52.9	55.9	1
ScII	5657.88	1.51	−0.49	41.7	44.1	1
ScII	5667.15	1.50	−1.19	13.7	13.9	1
ScII	5669.04	1.50	−1.07	16.7	17.8	1
ScII	5684.20	1.51	−1.00	18.4	20.4	1
ScII	6245.62	1.51	−1.11	16.0	17.6	2
ScII	6604.60	1.36	−1.30	15.6	16.3	1
VI	4875.49	0.04	−0.81	12.3	9.7	3
VI	5703.59	1.05	−0.20	5.8	5.3	3
VI	5727.06	1.08	+0.02	8.4	8.7	3
VI	6090.22	1.08	−0.05	7.7	7.4	3
CoI	5342.71	4.02	+0.54	7.7	7.3	2
CoI	5352.05	3.58	−0.10	5.2	4.4	2
CoI	5369.60	1.74	−1.47	11.6	10.3	2
CoI	5483.36	1.71	−1.49	12.1	11.1	4

Notes. [(a)]Astrophysically calibrated as explained in the text. [(b)]Equivalent widths for HD 22879. [(c)]Equivalent widths for HD 76932. **References.** (1) Lawler et al. (2019); (2) Prochaska et al. (2000); (3) Lawler et al. (2014); (4) Lawler et al. (2015).

Figure 1 shows a comparison of spectra near some typical Sc II, V I, and Co I lines for a high-α and a low-α star with similar $T_{\rm eff}$, logarithmic surface gravity log g, and [Fe/H], but a difference of 0.20 dex in [α/Fe]. As seen, the two stars have the same strengths of Cr I and Fe I lines, whereas the Sc II line is about 60% stronger in the high-α star (a small part of this is due to the difference in log g). The V I and Co I lines are also stronger in the high-α star, but the differences are not so large, and due to the weakness of these lines, it is more difficult to derive precise values of the differences in V and Co abundances.

The IRAF `splot` task was used to measure equivalent widths (EWs) of the Sc, V, and Co lines by Gaussian fitting to the line profiles in the spectra from Paper I. During the measurements, it was discovered that two low-α stars, HD 163810 and HD 250792 A, have somewhat asymmetric line profiles, clearly seen for the low-excitation V I lines. According to the Washington Visual Double Star Catalogue (Mason et al. 2020) both stars have 1–2 mag fainter components within 0.5 arcsec from the primary component, and because the derived [V/Fe] ratios are unusually high (about 0.20 dex higher than expected from the [V/Fe]–[Fe/H] relation for the other low-α stars), we have excluded the two stars from the discussion of abundances.

The Uppsala BSYN code was used to calculate EWs as a function of element abundance assuming LTE and taking hyper-fine splitting (HFS) into account according to the references given in Table 1. Interpolation to the observed EW then

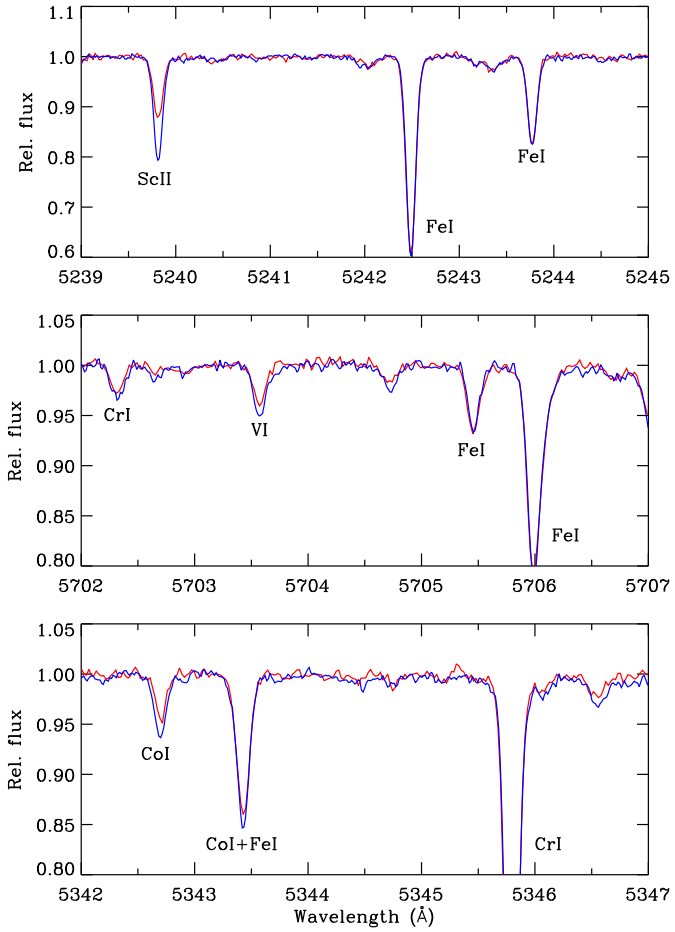

Fig. 1. Spectra near representative Sc, V, and Co lines for a high-α and a low-α star with similar $T_{\rm eff}$, $\log g$, and [Fe/H] values. The spectrum of G 159-50 ($T_{\rm eff}$ = 5713 K, $\log g$ = 4.44, [Fe/H] = −0.94, [α/Fe] = 0.32) is shown with a blue line, and that of CD −45 3283 ($T_{\rm eff}$ = 5685 K, $\log g$ = 4.61, [Fe/H] = −0.93, [α/Fe] = 0.12) with a red line.

yields the element abundance. First, two bright standard stars, HD 22879 and HD 76932, with well known photometric values of $T_{\rm eff}$ and $\log g$ were analysed differentially with respect to the Sun avoiding saturated lines or lines significantly blended in the solar flux spectrum. Adopting the derived mean [X/H] abundances for the standard stars and solar abundances A(Sc) = 3.14, A(V) = 3.90, and A(Co) = 4.94[2] from Asplund et al. (2021), an "inverted" abundance analysis of HD 22879 and HD 76932 then yields the $\log gf$ value of all lines as given in Table 1. With these $\log gf$ values, the abundances of the programme stars were derived.

Model atmospheres were interpolated from the plane parallel (1D) MARCS grid (Gustafsson et al. 2008) to the spectroscopic $T_{\rm eff}$, $\log g$, [Fe/H], and [α/Fe] values determined in Nissen et al. (2014). The $T_{\rm eff}$ values are about 100 K higher than those in Papers I and II, because revised photometric temperatures of the standard stars were adopted from Casagrande et al. (2010). With this change of the $T_{\rm eff}$ scale and the corresponding changes of $\log g$, we have also updated the abundances derived in Papers I and II, but the changes of [X/Fe] are within ±0.02 dex.

From the line-to-line abundance scatter and the changes in derived abundances, when changing the atmospheric parameters and the microturbulence $\xi_{\rm turb}$ with one-sigma uncertainties ($\sigma T_{\rm eff}$ = ±35 K, $\sigma \log g$ = ±0.05 dex, and $\sigma \xi_{\rm turb}$ = ±0.05 km s^{-1}), we estimate that the one-sigma error is ±0.03 dex for [Sc/Fe] and [Co/Fe] and ±0.04 dex for [V/Fe]. The errors of abundance ratios with respect to Mg are about 0.01 dex higher. We emphasise that these numbers are internal statistical errors; in addition, there may be systematic errors in the derived abundance ratios due to the adoption of 1D model atmospheres and the assumption of LTE as discussed in Sect. 4

The derived values of [Sc/H], [V/H], and [Co/H] are given in the online Table A.1 together with the atmospheric parameters of the stars.

3. Separation of accreted and in situ born stars

Figure 2 shows [Mg/Fe] together with [Sc/Fe], [V/Fe], and [Co/Fe] as a function of [Fe/H]. Using the same classification as in Paper I, based on the [Mg/Fe]–[Fe/H] diagram and the kinematics of the stars, we have divided stars with halo kinematics, that is, those having a total space velocity with respect to the Local Standard of Rest (LSR), $V_{\rm LSR}$ > 180 km s^{-1}, into high-α and low-α populations. They are shown with blue and red circles, respectively. Stars with typical thick-disk kinematics are shown with black triangles.

As seen from Fig. 2, the high-α halo stars and the thick-disk stars have well defined metallicity trends with no systematic offset between the two populations. The standard deviation relative to fitted second order polynomials is 0.033 dex for [Mg/Fe], 0.030 dex for [Sc/Fe], 0.039 dex for [V/Fe], and 0.026 dex for [Co/Fe]. This is close to the estimated one-sigma errors of the abundance ratios. Hence, there is no evidence of a cosmic scatter at a given [Fe/H] for the high-α population. This supports that the high-α halo and the thick-disk stars were formed in regions with a high star formation rate over a short time such that Ia SNe did not contribute to the chemical evolution.

While [Mg/Fe] is nearly constant for the high-α population, [Sc/Fe] shows a rising trend with increasing [Fe/H]. This suggests that Sc has metallicity dependent CC SNe yields. The two other odd-Z elements in Fig. 2, vanadium (Z = 23) and cobalt (Z = 27) have, however, nearly constant [X/Fe] ratios as a function of [Fe/H]. This is in agreement with the yield calculations for CC SNe by Kobayashi et al. (2006). According to their Table 3, the initial mass function (IMF) weighted yield of Sc increases with a factor of two from [Fe/H] ≃ −1.3 to [Fe/H] ≃ −0.7, whereas the yields of V and Co do not change significantly over the same metallicity range.

The increase in [Sc/Fe] for the high-α stars amounts to ∼0.15 dex, when [Fe/H] increases from −1.6 to −0.5. This gradient of [Sc/Fe] refers to 1D LTE abundances. In a recent work, Mashonkina & Romanovskaya (2022) have shown that non-LTE corrections of Sc abundances derived from Sc II lines are significant. For a sample of 56 main-sequence stars in the same $T_{\rm eff}$ range as our stars, they find that the average non-LTE correction increases by ∼0.08 dex, when [Fe/H] decreases from −0.5 to −1.6 dex (see Table 2 in Mashonkina & Romanovskaya 2022). If such non-LTE corrections are applied to our derived Sc abundances, the gradient of [Sc/Fe] is reduced by ∼50%. Clearly, it would be interesting to make a non-LTE study of the Sc II lines in Table 1 for our set of stars, preferably with 3D model atmospheres. Studies of non-LTE corrections for V and Co are also needed.

Figure 2 shows that the low-α population, defined as stars falling below the dashed line in the [Mg/Fe]–[Fe/H] diagram, is also well separated from the high-α population in the

[2] A(X) = log ($N_{\rm X}/N_{\rm H}$) + 12.0.

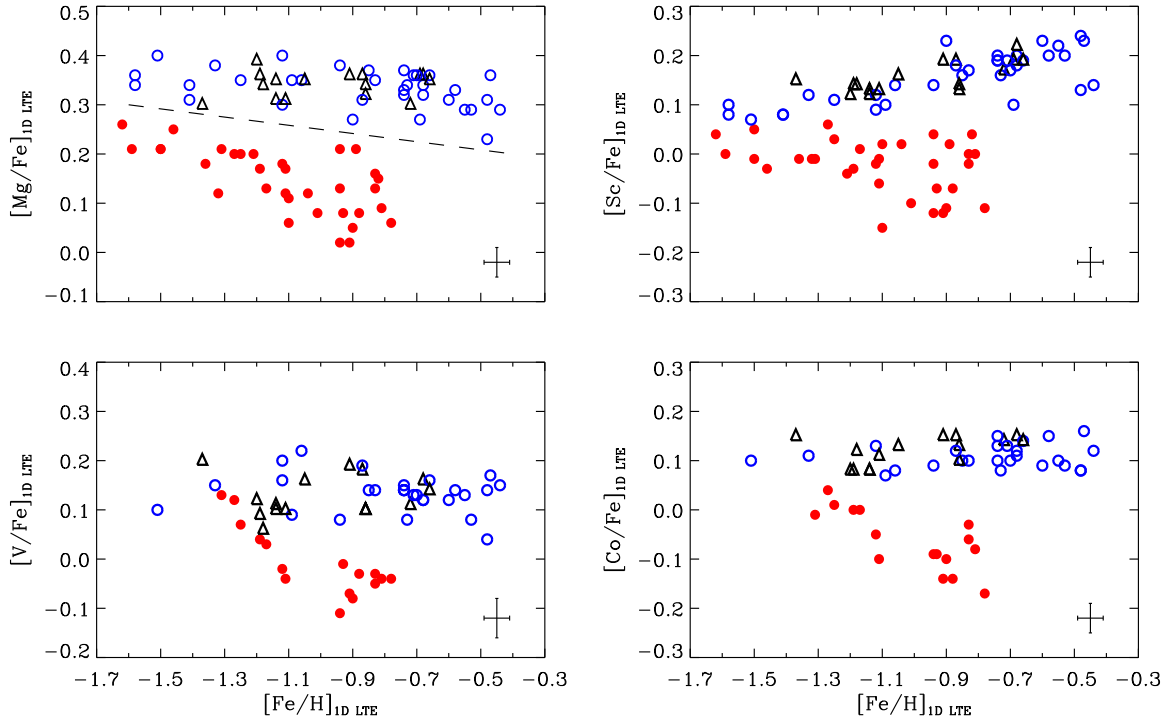

Fig. 2. [Mg/Fe], [Sc/Fe], [V/Fe], and [Co/Fe] versus [Fe/H]. Stars with halo kinematics are classified from the [Mg/Fe]–[Fe/H] diagram as belonging to either the high-α (blue circles) or the low-α (filled red circles) population. Stars with thick-disk kinematics are labelled with black triangles. The dashed line in the [Mg/Fe]–[Fe/H] diagram indicates the separation between high-α and low-α stars adopted in Paper I.

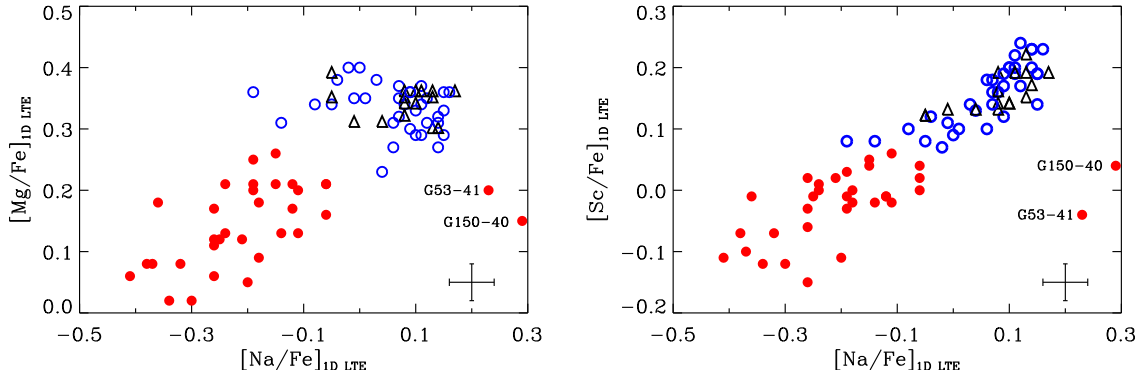

Fig. 3. [Mg/Fe] and [Sc/Fe] as a function of [Na/Fe] with the same symbols as in Fig. 2.

[Sc/Fe]–[Fe/H] diagram, although the separation is a bit smaller than the separation in [Mg/Fe]. The two populations are also well separated in [V/Fe] and [Co/Fe] in the metallicity range $-1.1 < \mathrm{[Fe/H]} < -0.7$, but for these two elements, the two sequences tend to merge at $\mathrm{[Fe/H]} \simeq -1.3$, whereas this happens at $\mathrm{[Fe/H]} \simeq -1.6$ for [Sc/Fe] and at an even lower metallicity in the case of [Mg/Fe].

As discussed in Paper II, there is a significant cosmic scatter in [X/Fe] among low-α stars with $\mathrm{[Fe/H]} \geq -1.1$, in particular for [Na/Fe], [Ni/Fe], and [Cu/Fe], for which the rms scatter in [X/Fe] is a factor ∼3 higher than the corresponding scatter for the high-α population (see Table 5 in Paper II). This can be explained if several merging dwarf galaxies with different star formation rates have contributed to the low-α accreted population. In the case of Sc, the rms scatter in [Sc/Fe] for the low-α stars with $\mathrm{[Fe/H]} \geq -1.1$ is 0.064 dex, that is, a factor ∼2 higher than the scatter in [Sc/Fe] for the high-α stars at a given [Fe/H]. For V and Co there are too few low-α stars to get a precise estimate of the dispersion in [V/Fe] and [Co/Fe].

Based on abundance data from the APOGEE survey, diagrams with [α/Fe] or [Mg/Mn] as a function of [Al/Fe] have proven to be very useful in separating accreted stars from in situ formed stars (e.g. Hawkins et al. 2015; Feuillet et al. 2021; Limberg et al. 2022; Fernandes et al. 2023). As mentioned above, we have not measured [Al/Fe], but one may instead use [Na/Fe] as shown in Paper II and by Buder et al. (2022) when selecting accreted stars in the Galactic Archaeology with HERMES (GALAH) survey. As seen from Fig. 3, the [Sc/Fe]–[Na/Fe] diagram can also be used for this purpose. Except for a small overlap among the more metal-poor ($\mathrm{[Fe/H]} < -1.4$) stars, high-α and low-α stars are well separated. Furthermore, there is a remarkably tight correlation between [Sc/Fe] and [Na/Fe] with the exception of two Na-rich stars, G 53-41 and G 150-40. These two stars have also exceptional low C and O abundances (Ramírez et al. 2012; Nissen et al. 2014) suggesting that they are second generation globular cluster escapees enriched in Na made through the CNO and Ne-Na cycles of hydrogen burning. Possible first-generation polluters are

intermediate-mass AGB stars (Ventura et al. 2001) or fast-rotating massive stars (Decressin et al. 2007).

4. 3D and non-LTE effects

In Sect. 5, the chemical evolution and nucleosynthesis of elements for the high-α and low-α populations are discussed based on trends in [X/Mg]–[Mg/H] diagrams. In this connection, consideration of possible 3D non-LTE effects is important, in particular for magnesium, because it is the reference element. We have, therefore, applied 3D non-LTE abundance corrections for the Mg I 5711.1 Å line, which is the only line used to derive Mg abundances in this paper[3]. The full details will be presented in a future study (Amarsi et al., in prep.). In brief, the calculations were carried out using `Balder` (Amarsi et al. 2018, 2022), which is a modified version of `Multi3D` (Leenaarts & Carlsson 2009). The model atom was that presented in Asplund et al. (2021). First, 1D non-LTE corrections were computed on a fine grid of `MARCS` models, a subset of those used in Amarsi et al. (2020) that covers the stellar parameters studied here. Secondly, 3D non-LTE versus 1D non-LTE corrections were applied to these based on calculations on a coarse grid of 1D and 3D models from the `Stagger`-grid (Magic et al. 2013), spanning 5000 K to 6500 K in $T_{\rm eff}$, 4.0 to 5.0 in $\log g$, −3.0 to 0.0 in [Fe/H], and −0.8 to 0.8 in [Mg/Fe]; the 1D calculations were performed for three values of microturbulence, namely 0, 1, and 2 km s^{-1}.

The corrections of [Mg/H] range from −0.03 dex for the coolest stars to +0.07 dex for the warmest and most metal-poor stars. We stress that these are differential corrections: the 3D non-LTE correction for the Sun (+0.057 dex) has been subtracted out. The corrections have some effect on the slopes of the [X/Mg]–[Mg/H] relations, which are increased by 0.05–0.10 relative to the values obtained without the 3D non-LTE corrections. At a given [Mg/H], the difference in [X/Mg] between the low-α and high-α stars is, however, not changed significantly.

For the C and O abundances, we have used the 3D non-LTE values presented in Amarsi et al. (2019). For Na, Si, and Ca, new 1D non-LTE calculations were performed with `Balder` on a fine grid of `MARCS` models covering the stellar parameters and spectral lines studied here[4]. The sodium atom was that presented in Lind et al. (2011) and the calcium atom that presented in Asplund et al. (2021); they were recently also applied in Barklem et al. (2021) and Skúladóttir et al. (2021), respectively. The silicon atom was based on that used in Amarsi & Asplund (2017). Here, the atom was updated to use inelastic hydrogen collisions based on the asymptotic model of Barklem (2016) combined with the free electron model of Kaulakys (1991) in the scattering length approximation as described in Amarsi et al. (2018). The reduced model atom is also more complex than before due to the inclusion of fine structure levels up to 7 eV above the ground state.

While the differential 3D non-LTE corrections of [O/H] derived from the O I 7774 Å triplet range from −0.05 to +0.10 dex for our sample of stars, the 1D non-LTE corrections of [Na/H], [Si/H], and [Ca/H] are less significant. The differential corrections range from −0.03 to +0.04 dex for [Na/H], from −0.01 to +0.01 dex for [Si/H], and from 0.00 to +0.07 dex for [Ca/H].

Furthermore, we have have applied 1D non-LTE corrections for Mn from Bergemann et al. (2019) using `Spectrum Tools`[5] to interpolate to the atmospheric parameters of our stars. The metallicity trend of [Mn/Fe] is very sensitive to these corrections; Eitner et al. (2020) found that the [Mn/Fe]–[Fe/H] trend becomes nearly flat when applying the Bergemann et al. (2019) corrections. In our case, the differential non-LTE corrections of [Mn/H] range from ∼0.0 dex for the coolest stars to about +0.20 dex for the warmer and most metal-poor stars in the sample.

For Cu, we have adopted the abundances derived in the 1D non-LTE re-analysis of Cu I lines from Paper II by Yan et al. (2016). As in the case of Mn, this leads to a less steep slope of the [Cu/Mg]–[Mg/H] relation than obtained with LTE abundances.

As a number of suitable Ti II, Cr II, and Fe II lines are available in our spectra, we have used these lines to derive abundances. This has the advantage that non-LTE effects are estimated to be insignificant (Bergemann & Cescutti 2010; Bergemann 2011; Lind et al. 2012). In the case of Fe, we used 3D abundances from Amarsi et al. (2019), but the 3D–1D difference have an rms scatter of only 0.017 dex. The Ti and Cr abundances were derived from 1D models.

For the remaining elements (Sc, V, Co, Ni and Zn) we do not have 3D and/or non-LTE corrections available for the spectral lines used to determine abundances. To the extent that the corrections depend on metallicity, the slopes of the [X/Mg]–[Mg/H] relations may, therefore, be incorrect (see discussion of Sc in Sect. 3). For all the elements discussed above, the mean difference in [X/Mg] between the low-α and the high-α stars is, however, practically independent on whether 3D and/or non-LTE corrections are applied or not. This is because the average $T_{\rm eff}$ and $\log g$ values of the two populations are about the same.

The final abundances are given in the online Table A.1. This table also includes the 3D non-LTE corrections for Mg and the 1D non-LTE corrections for Na, Si, Ca, and Mn abundances. The 3D non-LTE corrections for C and O abundances and the 3D corrections for Fe abundances derived from Fe II lines may be obtained from Amarsi et al. (2019) and the 1D non-LTE corrections for Cu abundances from Yan et al. (2016).

5. Nucleosynthesis of the elements

Predictions from Galactic chemical evolution (GCE) models are normally compared to observed [X/Fe]–[Fe/H] relations. The choice of Fe as a reference element is connected to the fact that iron has far the largest set of lines in spectra of late-type stars and is therefore usually the element with the most precise stellar abundances. Iron has, however, significant yield contributions from both CC and Ia SNe, which complicates the interpretation of the [X/Fe]–[Fe/H] relations. As shown by Weinberg et al. (2019, 2022) based on APOGEE abundances, it is more straightforward to use a reference element that is produced almost entirely in CC SNe, such as O or Mg. They found that the thick and the thin disk populations in the Milky Way have different [X/Mg] versus [Mg/H] relations, but for each population the relation is nearly constant throughout the disk. This is not the case for the trends of [X/Fe] versus [Fe/H].

Following the approach of Weinberg et al. (2019), we show in Fig. 4 the [X/Mg]–[Mg/H] relations for high-α and low-α stars in the $-1.4 <$ [Mg/H] < -0.4 range, where the two populations overlap. As seen, there is no significant difference in the

[3] In Paper I, the Mg I 4730.0 Å line was included for stars observed with the NOT/FIES spectrograph.

[4] Table 3 in Paper II contains a list of all spectral lines used to determine abundances.

[5] `http://nlte.mpia.de`.

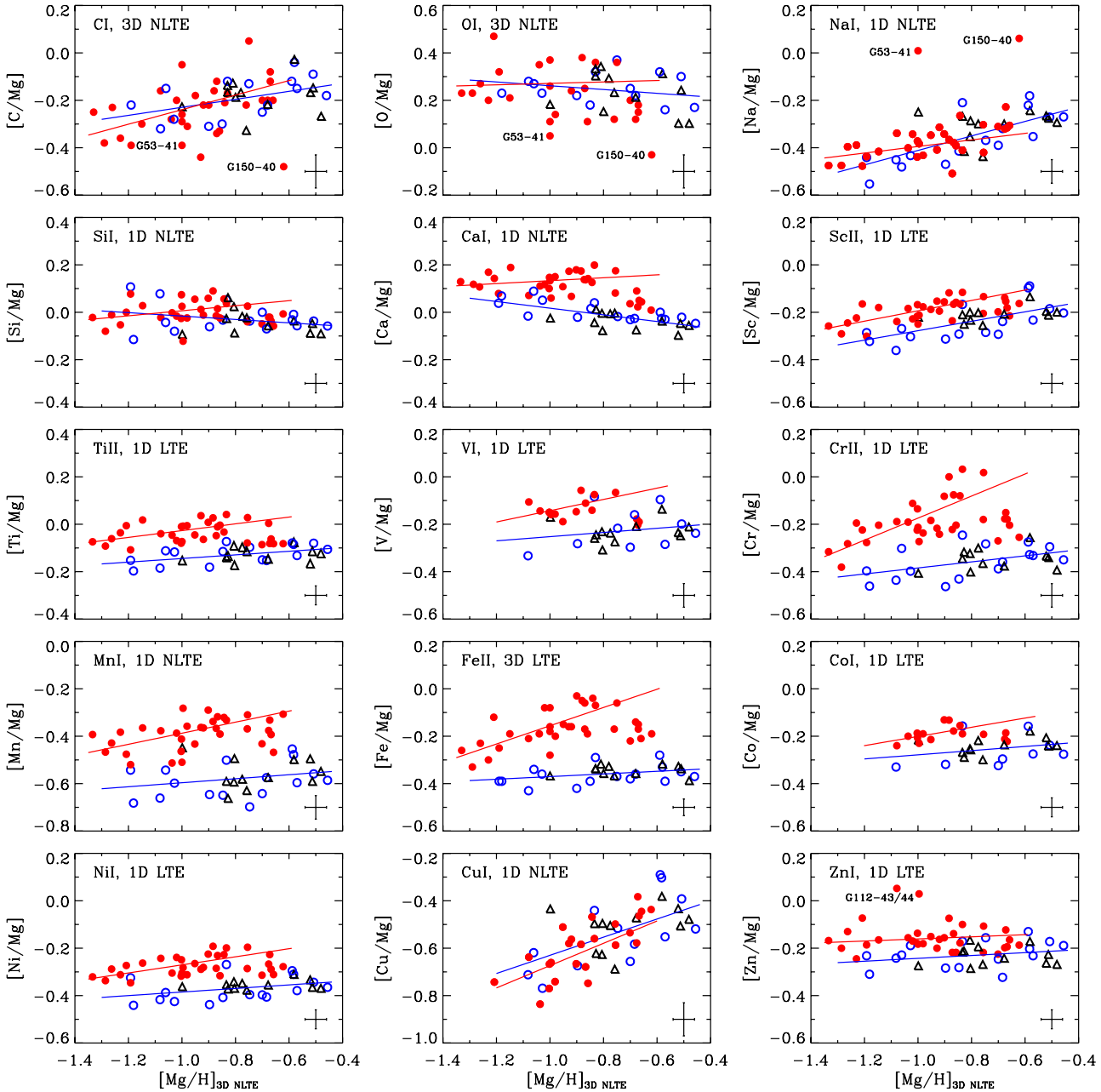

Fig. 4. [X/Mg] as a function of [Mg/H] with the same symbols as in Fig. 2. The blue lines show least-squares fits to the high-α stars and the red lines show fits to the low-α stars after excluding stars probably associated with the Thamnos substructure (see Fig. 5). On each panel, the atomic species of spectral lines used for deriving abundances and the method of analysis are indicated.

[X/Mg]–[Mg/H] relations of the high-α and low-α populations for C, O, Na, and Cu, whereas the largest difference between the two populations is seen for Cr, Mn, and Fe. This suggests that C, O, Na, and Cu have no contribution from Ia SNe, whereas Cr, Mn, and Fe get the largest Ia contribution. The remaining elements represent intermediate cases. In Sect. 5.2, we present a more detailed investigation of this scenario, but first we discuss the possible existence of substructure in the [X/Mg]–[Mg/H] relations for the low-α population.

5.1. Substructure in the low-α population

As mentioned in Sect. 3, there is a significant cosmic scatter in [Na/Fe], [Sc/Fe], [Ni/Fe], and [Cu/Fe] among the low-α stars. The dispersion in some of the abundance ratios shown in Fig. 4 is also higher than expected from the measurement error, most notable in the case of [Fe/Mg] for which the standard deviation around the linear fit is 0.070 dex for the low-α population compared to 0.033 dex for the high-α stars. The main contribution to this higher dispersion comes from a splitting of stars with [Mg/H] ~ -0.8 into two groups, that is, six high-[Fe/Mg] stars labelled with circles in Fig. 5 and seven low-[Fe/Mg] stars labelled with squares (see list in Table 2). The same distribution is present for [Cr/Mg] as seen in the upper right panel of Fig. 5. Interestingly, this substructure is only clearly seen after applying the 3D non-LTE corrections for Mg (Lind & Amarsi 2024).

It could be that the substructure in [Fe/Mg] and [Cr/Mg] is due to errors in the Mg abundances, but a similar substructure is seen if we replace Mg with Na as the reference element and

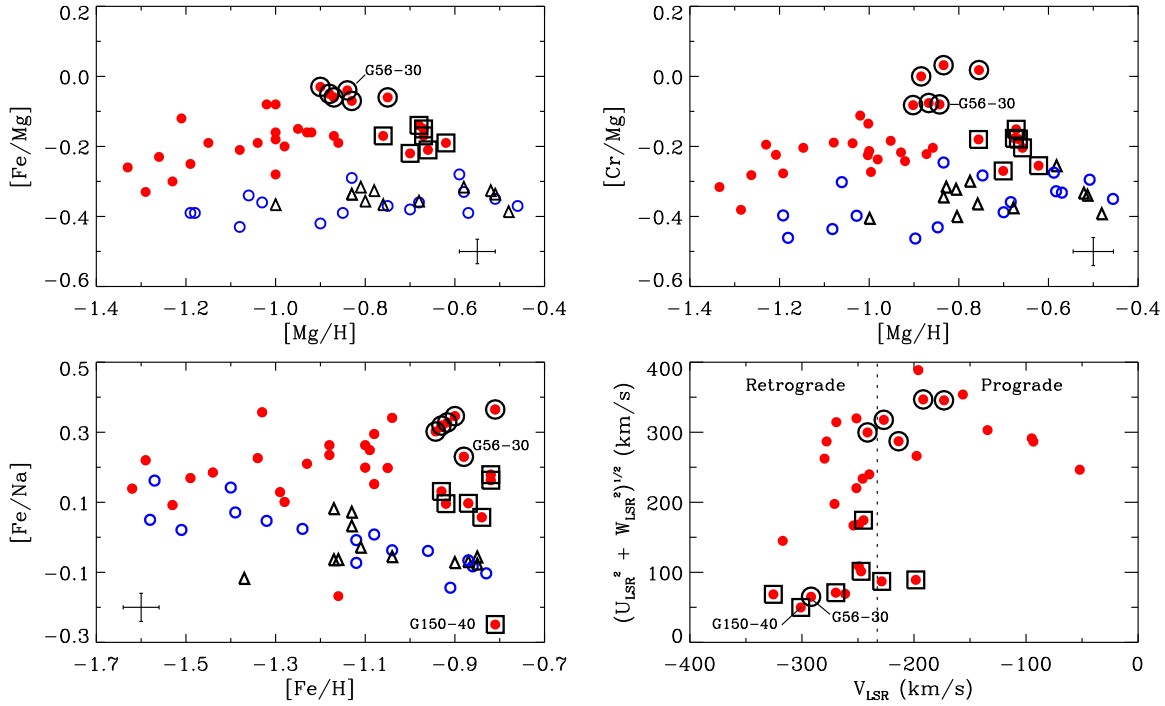

Fig. 5. Substructure in the distribution of [Fe/Mg], [Cr/Mg], and [Fe/Na] for low-α stars with [Mg/H] $\simeq -0.8$. Stars with high [Fe/Mg] values are labelled with black circles and those with lower [Fe/Mg] values with squares. In the lower right panel, the Toomre diagram for the low-α stars is shown with the same labelling.

Table 2. Abundance ratios and kinematics of high-[Fe/Mg] and low-[Fe/Mg] stars in the low-α population.

ID	$[\frac{Mg}{H}]$	$[\frac{Fe}{Mg}]$	$[\frac{Cr}{Mg}]$	$[\frac{Fe}{Na}]$	U_{LSR} (km s^{-1})	V_{LSR} (km s^{-1})	W_{LSR} (km s^{-1})
High-[Fe/Mg] stars							
CD−45 3283	−0.88	−0.05	−0.00	0.32	−302	−227	−98
CD−57 1633	−0.87	−0.06	−0.07	0.32	−298	−241	−32
G 56-30	−0.84	−0.04	−0.08	0.23	35	−292	−55
G 66-22	−0.83	−0.07	0.03	0.35	−285	−214	31
G 82-05	−0.75	−0.06	0.01	0.37	−343	−173	40
G 121-12	−0.90	−0.03	−0.08	0.31	−330	−192	106
Low−[Fe/Mg] stars							
G 46-31	−0.67	−0.15	−0.18	0.16	32	−326	61
G 56-36	−0.70	−0.22	−0.27	0.09	−101	−247	8
G 98-53	−0.66	−0.21	−0.20	0.09	−151	−245	−87
G 150-40	−0.62	−0.19	−0.26	−0.25	−49	−301	11
G 170-56	−0.76	−0.17	−0.18	0.13	−61	−270	−36
HD 103723	−0.68	−0.14	−0.17	0.18	−70	−198	55
HD 105004	−0.67	−0.17	−0.15	0.06	−36	−229	−79

use [Fe/H] instead of [Mg/H] on the abscissa (lower left panel of Fig. 5) except that one high-[Fe/Mg] star, G56-30, falls between the two groups, and the Na-rich star, G150-40, is shifted to a very low value of [Fe/Na].

In order to see if the substructure in the abundance diagrams of Fig. 5 is related to the kinematics of the stars, we have plotted all low-α stars in the Toomre velocity diagram shown in the lower right panel of Fig. 5. The space velocities with respect to the LSR were calculated based on *Gaia* DR3 data as described in detail by Nissen et al. (2021); typical errors of the velocity components are 1–2 km s^{-1}.

Five of the six high-[Fe/Mg] stars fall in the same high-energy region of the Toomre diagram as stars accreted from the GSE dwarf galaxy (Belokurov et al. 2018; Helmi et al. 2018); they have large (negative) values of U_{LSR} (see Table 2) and V_{LSR} close to the value dividing prograde from retrograde moving stars, $V_{LSR} = -233$ km s^{-1} (McMillan 2017). The exception is G 56-30, the star with an intermediate value of [Fe/Na]. Six of the seven low-[Fe/Mg] stars are, on the other hand, situated in the low-energy part of the Toomre diagram and the majority are retrograde moving. We suggest that they belong to the Thamnos substructure identified by Koppelman et al. (2019). Interestingly,

Table 3. Coefficients of the linear fits, [X/Mg] = $a + b$ ([Mg/H] + 0.8), shown in Fig. 4, and the derived CC and Ia SN yields.

	High-α stars		Low-α stars				
X	a	b	a	b	F_X	$[X/Fe]_{CC}$	$[X/Fe]_{Ia}$
C	−0.196 ± 0.015	+0.17 ± 0.07	−0.178 ± 0.035	+0.31 ± 0.13			
O	+0.245 ± 0.015	−0.08 ± 0.07	+0.277 ± 0.042	+0.03 ± 0.14	0.08 ± 0.13	+0.60 ± 0.06	
Na	−0.350 ± 0.013	+0.31 ± 0.06	−0.367 ± 0.018	+0.14 ± 0.07			
Mg					0.00	+0.36 ± 0.06	
Si	−0.030 ± 0.010	−0.07 ± 0.05	+0.028 ± 0.015	+0.11 ± 0.06	0.16 ± 0.06	+0.33 ± 0.07	−0.47 ± 0.18
Ca	−0.011 ± 0.006	−0.14 ± 0.03	+0.146 ± 0.013	+0.06 ± 0.05	0.48 ± 0.06	+0.34 ± 0.07	+0.02 ± 0.09
Sc	−0.238 ± 0.009	+0.20 ± 0.04	−0.150 ± 0.012	+0.22 ± 0.05			
Ti	−0.129 ± 0.006	+0.08 ± 0.03	+0.002 ± 0.012	+0.14 ± 0.05	0.39 ± 0.05	+0.23 ± 0.07	−0.18 ± 0.09
V	−0.235 ± 0.016	+0.09 ± 0.09	−0.095 ± 0.017	+0.24 ± 0.11	0.42 ± 0.09	+0.13 ± 0.10	−0.25 ± 0.14
Cr	−0.359 ± 0.010	+0.13 ± 0.05	−0.081 ± 0.024	+0.47 ± 0.09	0.99 ± 0.18	+0.00 ± 0.07	+0.00 ± 0.10
Mn	−0.579 ± 0.013	+0.08 ± 0.06	−0.341 ± 0.019	+0.23 ± 0.07	0.81 ± 0.13	−0.22 ± 0.07	−0.31 ± 0.10
Fe	−0.359 ± 0.006	+0.06 ± 0.03	−0.079 ± 0.020	+0.39 ± 0.08	1.00	0.00	0.00
Co	−0.261 ± 0.012	+0.09 ± 0.07	−0.162 ± 0.014	+0.19 ± 0.09	0.28 ± 0.06	+0.10 ± 0.10	−0.45 ± 0.14
Ni	−0.370 ± 0.007	+0.08 ± 0.04	−0.236 ± 0.012	+0.17 ± 0.05	0.40 ± 0.06	−0.01 ± 0.10	−0.41 ± 0.12
Cu	−0.554 ± 0.022	+0.38 ± 0.11	−0.579 ± 0.036	+0.47 ± 0.20			
Zn	−0.231 ± 0.009	+0.06 ± 0.04	−0.152 ± 0.015	+0.05 ± 0.06	0.22 ± 0.06	+0.13 ± 0.10	−0.53 ± 0.15

both Koppelman et al. (2019) and Horta et al. (2023) find evidence from APOGEE abundances that Thamnos stars have [Mg/Fe] between the mean values of [Mg/Fe] for GSE and high-α stars, respectively, in agreement with our results. Hence, both the abundance ratios and the kinematics point to the existence of two groups of accreted stars among our more metal-rich low-α stars, that is, debris stars from the GSE and Thamnos dwarf galaxies.

The abundance ratios shown in Fig. 5 suggest that the contribution from Ia SNe to the chemical evolution was more important at a given [Mg/H] in the GSE galaxy than in the Thamnos dwarf galaxy. When discussing the nucleosynthesis of elements in the following sections this will be taken into account. Therefore, Fig. 4 shows linear least-squares fits to the low-α stars after excluding the seven Thamnos stars. Furthermore, the two C- and O-poor, Na-rich stars in the C, O, and Na panels and the Zn-rich binary star G 112-43/44 in the Zn panel (Nissen et al. 2021) have been excluded from the fits. Coefficients for the fits are given in Table 3.

5.2. Empirical supernova yields

Adopting notations used by Weinberg et al. (2017) in their analytic one-zone GCE models for the abundance of an element X in the interstellar gas due to prompt CC SNe and delayed Ia SNe enrichment, the change in [X/Mg] relative to the early-time (t_0) CC plateau is

$$\Delta[X/Mg] = \log \frac{Z_X^{CC}(t) + Z_X^{Ia}(t)}{Z_{Mg}^{CC}(t)} - \log \frac{Z_X^{CC}(t_0)}{Z_{Mg}^{CC}(t_0)}. \quad (1)$$

Here $Z_X^{CC}(t)$ and $Z_X^{Ia}(t)$ are the abundances of element X produced by CC and Ia SNe, respectively, and it is assumed that only CC SNe contribute to Mg.

Assuming that the IMF integrated CC yield, m_X^{CC}, is constant in time, that is, independent of metallicity, we have

$$\frac{Z_X^{CC}(t)}{Z_{Mg}^{CC}(t)} = \frac{Z_X^{CC}(t_0)}{Z_{Mg}^{CC}(t_0)} = \frac{m_X^{CC}}{m_{Mg}^{CC}}. \quad (2)$$

Equation (1) then yields

$$\Delta[X/Mg] = \log\left(1 + \frac{Z_X^{Ia}(t)}{Z_X^{CC}(t)}\right), \quad (3)$$

and as a special case with X = Fe

$$\Delta[Fe/Mg] = \log\left(1 + \frac{Z_{Fe}^{Ia}(t)}{Z_{Fe}^{CC}(t)}\right), \quad (4)$$

which corresponds to Eq. (42) in Weinberg et al. (2017) when replacing Mg with O as the CC reference element.

Assuming that the SNe Ia yield, m_X^{Ia}, is also independent of metallicity and introducing the ratio between Ia and CC SNe yields divided by the same ratio for Fe, i.e.

$$F_X = \frac{m_X^{Ia}/m_X^{CC}}{m_{Fe}^{Ia}/m_{Fe}^{CC}}, \quad (5)$$

we get

$$\Delta[X/Mg] = \log\left(1 + F_X(10^{\Delta[Fe/Mg]} - 1)\right). \quad (6)$$

corresponding to Eq. (10) in Feuillet et al. (2018) when Mg is replaced with O.

Solving Eq. (6) with respect to F_X we get

$$F_X = \frac{10^{\Delta[X/Mg]} - 1}{10^{\Delta[Fe/Mg]} - 1}. \quad (7)$$

Introducing logarithmic yields, $[X/Fe]_{CC}$ and $[X/Fe]_{Ia}$, we get from Eq. (5)

$$[X/Fe]_{Ia} = [X/Fe]_{CC} + \log F_X. \quad (8)$$

$[X/Fe]_{CC}$ is determined as the mean value of [X/Fe] for the high-α stars and is given in Col. 7 of Table 3. For elements having a significant slope of [X/Mg] versus [Mg/H] (Na, Sc, and Cu) no value is given. These elements have metallicity dependent CC SNe yields and Eqs. (2)–(8) are therefore not valid. Furthermore, the value of $[C/Fe]_{CC}$ is omitted, because carbon

probably gets a significant contribution from intermediate-mass AGB stars at [Fe/H] $\gtrsim -1.5$ (Kobayashi et al. 2020, Fig. 5).

The standard deviation of the mean value of $[X/Fe]_{CC}$ ranges from 0.005 dex for Ni to 0.013 dex for O, but systematic uncertainties are much larger. The high precision of the stellar abundances were obtained by determining $T_{\rm eff}$, $\log g$, and [X/Fe] spectroscopically relative to two bright standard stars, HD 22879 and HD 76932. Hence, the error of $[X/Fe]_{CC}$ is determined by the uncertainty of the standard star abundances relative to the solar abundances. Due to the uncertainty of the photometric parameters of the standard stars ($\sigma T_{\rm eff} = \pm 50$ K and $\sigma \log g = \pm 0.05$ dex) and the difficulty of measuring accurate equivalent widths of lines in the crowded solar flux spectrum, we estimate that the error of $[X/Fe]_{CC}$ is ~0.05 dex. In addition, there is a potential error of $[X/Fe]_{CC}$ for elements for which the derived abundances were not corrected for 3D non-LTE effects. In the case of elements having full 3D non-LTE corrections available, we find that such corrections lead to changes of +0.038 dex for $[O/Fe]_{CC}$ and +0.019 dex for $[Mg/Fe]_{CC}$. For elements with 1D non-LTE corrections, the changes of $[X/Fe]_{CC}$ are +0.002 dex for Si, +0.028 dex for Ca, and as much as +0.081 dex for Mn. Guided by these numbers, we adopt errors of $[X/Fe]_{CC}$ ranging from ±0.06 dex for elements with full 3D non-LTE corrections (O and Mg) and ±0.10 dex for elements with no correction (V, Co, Ni, and Zn). For the remaining elements that have non-LTE corrections (Si, Ca, and Mn) or have abundances determined from ionised lines (Ti and Cr), we adopt an error of ±0.07 dex for $[X/Fe]_{CC}$.

The F_X values are determined from Eq. (7) using Δ[X/Mg] measured at [Mg/H] = −0.8, that is, the difference of the a-coefficients for the linear fits to the low-α and high-α stars. The resulting values are given in Col. 6 of Table 3 together with the 1-σ errors derived from the errors of the a-coefficients. In this connection, we note that the systematic errors of [X/Fe] discussed above do not affect Δ[X/Mg] significantly, because low-α and high-α stars are affected in the same way.

Finally, empirical Ia SNe yields are determined from Eq. (8). Values are given in Col. 8 of Table 3 except for O and Mg. Magnesium was assumed to be a pure CC element, i.e. $F_X = 0$, and the F_X value of O is not significantly different from zero indicating that the Ia yield is very small relative to the CC yield.

5.3. Comparison of empirical and predicted SN yields

A complete comparison between our empirical yields and yields calculated for models of SNe is outside the scope of this paper. We may, however, provide some examples to show how the empirical yields can be used to constrain parameters of the models. As a measure of the success of the comparison we use the reduced chi-square

$$\chi^2_r = \frac{1}{N} \sum_{i=1}^{N} ([X/Fe]_{i,\rm pre} - [X/Fe]_{i,\rm emp})^2 / \sigma^2_{i,\rm emp}, \quad (9)$$

where $[X/Fe]_{i,\rm pre}$ and $[X/Fe]_{i,\rm emp}$ are the predicted and empirical yields, respectively, for an element i, and $\sigma_{i,\rm emp}$ is the estimated error of the empirical yield. N is the number of elements, i.e. $N = 11$ for the CC yields and $N = 9$ for the Ia yields according to Table 3.

The empirical CC yields were compared with yields calculated by Kobayashi et al. (2006, 2020) and Limongi & Chieffi (2018) for spherical models with a metallicity of $Z = 0.1\,Z_\odot$, close to the mean Z for our stars. As discussed in these papers, assumptions about formation of remnants (neutron stars or black holes) are critical for the yield calculations. Limongi & Chieffi (2018) have three sets of models: "set F" in which the stars are assumed to eject 0.07 $M_\odot$ ^{56}Ni (decaying to ^{56}Fe), "set M", which is based on the mixing and fallback scheme of Umeda & Nomoto (2002), and "set R", which is the same as "set M" for stars with masses in the range 13–25 $M_\odot$, while more massive stars are assumed to collapse to black holes and only contribute to the yields via stellar winds. Total yields were obtained by integrating over the Salpeter (1955) IMF from 13 to 120 $M_\odot$ and are converted to [X/Fe] values using the Asplund et al. (2021) solar abundances. In Kobayashi et al. (2006, K06), the mass cuts are chosen so that 0.07 $M_\odot$ ^{56}Fe is produced by normal Type II SNe, and yields from high-energy SNe, so-called hypernovae (HNe), are included. The parameters of the mixing and fallback scheme for HNe are constrained to provide a yield of [O/Fe] = 0.5 and a relative HNe fraction of 0.5 for $M \geq 20\,M_\odot$ is assumed. Total yields are found by integration over the Salpeter IMF from 13 to 50 $M_\odot$. The yields in Kobayashi et al. (2020, K20) represent an update of the K06 yields and adoption of the Kroupa (2008) IMF.

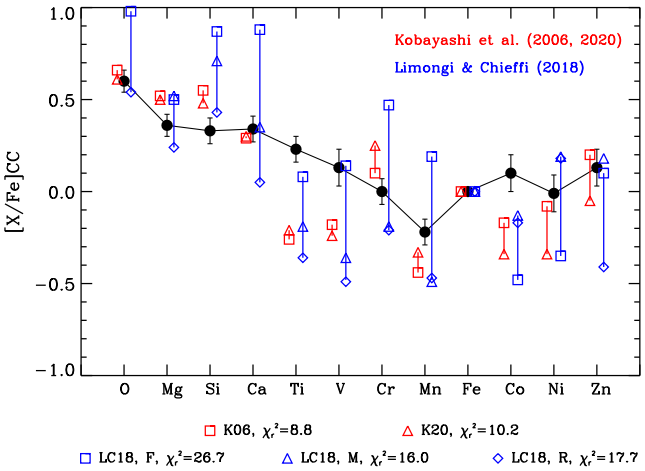

Fig. 6. Comparison of empirical $[X/Fe]_{CC}$ yields with IMF integrated yields predicted from models of CC SNe. The empirical yields are shown with filled black circles. Yields predicted from the models of Kobayashi et al. (2006; 2020, K06 and K20) are plotted with red symbols and yields calculated from Limongi & Chieffi (2018, LC18, models F, M, and R) with blue symbols; see text for details. For each model, the reduced chi-square for the comparison with the empirical yields is given.

As seen from Fig. 6, all models give a poor fit to the empirical CC yields, i.e. $\chi^2_r \gg 1$. The Limongi & Chieffi models show large differences in the yields[6] and have $\chi^2_r \geq 16$. The Kobayashi et al. models perform somewhat better, but the predicted yields of Ti, V, and Co are much lower than the empirical yields leading to $\chi^2_r \sim 10$. As discussed by Kobayashi et al. (2020), the yields of Ti, V, and Co are sensitive to multidimensional effects. Based on 2D models with jets (Maeda & Nomoto 2003; Tominaga 2009), it was estimated that the yields of Ti, V, and Co should be increased by 0.45, 0.2, and 0.2 dex, respectively. This decreases the reduced chi-square to $\chi^2_r \sim 4$.

Figure 7 shows a comparison of the empirical Ia SNe yields with yields calculated for near-$M_{\rm Ch}$ and sub-$M_{\rm Ch}$ models having $Z = 0.1\,Z_\odot$. Included are yields from Leung & Nomoto (2018)

[6] We have adopted yields from Limongi & Chieffi (2018) for models with an initial rotation velocity $V = 0$ km s^{-1}; models with higher values, $V = 150$ and 300 km s^{-1}, have similar high χ^2_r values.

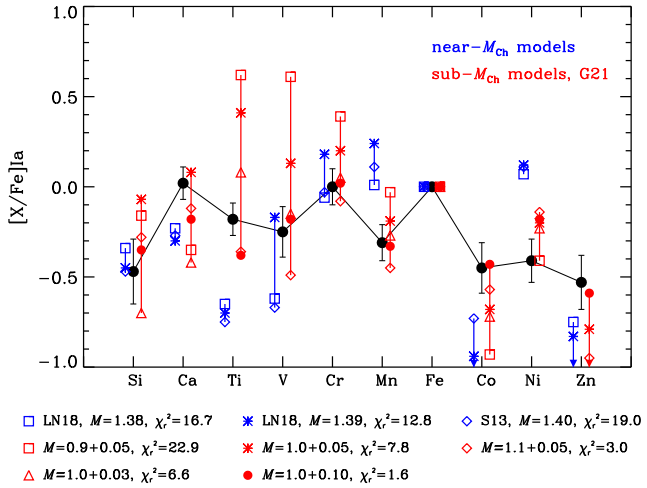

Fig. 7. Comparison of empirical $[X/Fe]_{Ia}$ yields with yields predicted from models of Ia SNe. The empirical yields are shown with filled black circles. Yields predicted from near-M_{Ch} models of Leung & Nomoto (2018, LN18) and Seitenzahl et al. (2013, S13) are plotted with blue symbols and yields calculated from sub-M_{Ch} models of Gronow et al. (2021, G21) with red symbols. The core masses and masses of the He envelope for the sub-M_{Ch} models are given in units of the mass of the Sun. For each model, the reduced chi-square for comparison with the empirical yields is given.

for two near-M_{Ch} deflagration-to-detonation models with masses at explosion, $M = 1.38$ and $1.39\,M_\odot$, and hence different core densities ($\rho_c = 3 \times 10^9$ g cm^{-3} and $\rho_c = 5 \times 10^9$ g cm^{-3}), and yields from a similar model with $M = 1.40\,M_\odot$ and $\rho_c = 2.9 \times 10^9$ g cm^{-3} by Seitenzahl et al. (2013). The sub-M_{Ch} yields all refer to models by Gronow et al. (2021) of double detonation white dwarfs with different masses of the C-O core and the He-shell as shown in the figure.

As seen from Fig. 7, the yields of the three near-M_{Ch} models give a poor fit to the empirical yields; the predicted yields for Ca and Ti are too low and those of Mn and Ni are too high, leading to $\chi_r^2 > 12$. The sub-M_{Ch} models of Gronow et al. (2021) have large differences in the predicted yields, depending on the masses of the C-O core and the He-shell, but the model with a core mass of $M = 1.0\,M_\odot$ and a He-shell mass of $M = 0.10\,M_\odot$ has a reduced chi-square of $\chi_r^2 = 1.6$ only. As seen, the predicted yields for this model (filled red circles in Fig. 7) do not deviate more than two-sigma from the empirical yields. This suggests that a dominant contribution from sub-M_{Ch} Ia SNe is needed to explain the chemical evolution of the GSE dwarf galaxy as was also found by Sanders et al. (2021) based on [Mn/Fe] and [Ni/Fe] ratios.

5.4. Comparison to dSph galaxies

The abundance pattern of the low-α population, which comes from disrupted dwarf galaxies, is in good general agreement with results from surviving satellite dwarf spheroidal (dSph) galaxies around the Milky Way; at least for those dSph galaxies with relatively short star formation histories, comparable to that expected for GSE. A detailed abundance pattern for stars in the Sculptor dSph galaxy was provided in the work of Hill et al. (2019). They used the increase in [X/Mg] with [Fe/H] to estimate the relative Ia SNe contribution to each element (their Fig. 14). They found the strongest impact of Ia SNe on the elements Cr, Mn, Fe, which showed similar slopes in excellent agreement with our results (Fig. 4). Furthermore, they found a modest but significant contribution of Ia SNe to the elements S, Ca, Ti, Sc, and Co, while the results for Ni and Zn hinted at a small contribution but were less conclusive. This is consistent with the low-α population presented here.

Analyses of dSph galaxies have also been used to study the nature of low-metallicity Ia SNe. Kirby et al. (2019) used the abundances of Mg, Si, Ca, Cr, Co, Ni, and Fe to try and understand the impact of Ia SNe in five dSph galaxies: Sculptor, Leo II, Draco, Sextans, and Ursa Minor. Based mainly on the [Ni/Fe] abundances, Kirby et al. (2019) concluded that the dominant Ia SNe channel in ancient dSph galaxies is that of sub-M_{ch} white dwarfs, as found here via the low-α population; however this might differ for galaxies with more extended star formation histories. Other works have focused on fewer stars and/or fewer elements, but those targeting Mn all suggested a significant contribution of Ia SNe to Mn, pointing to sub-M_{ch} white dwarfs as the dominant Ia SNe channel, with possibly also significant contribution of Type Iax SNe (North et al. 2012; Cescutti & Kobayashi 2017; de los Reyes et al. 2020).

5.5. Disentangling PISNe and Ia SNe

The results presented in Fig. 4 can be used to check for descendants of so-called Pair Instability Supernovae (PISNe), which have been predicted to be the death of massive zero-metallicity stars of $150 \leq M_\star/M_\odot \leq 260$ (e.g. Heger & Woosley 2002). The abundance pattern of such stars is very unique, with very little production of odd-Z elements, resulting in a strong odd-even effect. The surviving descendants are predicted to be very rare, only <0.1% of Milky Way halo stars at [Fe/H] ≈ -1 are expected to have received >50% of their metals from PISNe (de Bennassuti et al. 2017). Therefore it is unsurprising that no star in our sample shows evidence of such imprint.

Our sample can, however, be used as an empirical benchmark for the abundance pattern of early Ia SNe, which overlaps to a certain degree with that predicted for PISNe. In particular, low abundances of the elements Na and Cu relative to Ca or Fe have been identified as a clear signature of PISNe (Salvadori et al. 2019). However, our results show very clearly that low-metallicity Ia SNe do not produce Na and Cu; the [X/Mg] versus [Mg/H] trends for these two elements are the same for low- and high-α stars. It is therefore clear that a star which would be dominantly enriched by an early Type Ia supernova, without much CC SNe contribution, would also have low Na and Cu abundances.

There are, however, some key differences between the abundance patterns of PISNe and Ia SNe. As seen from Fig. 3 in Salvadori et al. (2019), the production of Co and Zn by PISNe in the mass range $150 \leq M_\star/M_\odot \leq 260$ is very low compared to the production of Ni, i.e. $[Co/Ni]_{PISN} < -0.6$ and $[Zn/Ni]_{PISN} < -1.3$. As seen from Figs. 6 and 7, the empirical yields of these abundance ratios are significantly higher both for CC and Ia SNe, i.e. $[Co/Ni]_{CC} > -0.10$, $[Co/Ni]_{Ia} > -0.30$, $[Zn/Ni]_{CC} > -0.10$, and $[Zn/Ni]_{Ia} > -0.40$. Hence, it should be possible to find signatures of PISNe by measuring accurate Co, Ni, and Zn abundances. We note, in this connection, that two stars, for which imprints of PISNe have been suggested, i.e. SDSS J0018-0939 (Aoki et al. 2014) and LAMOST 1010+2358 (Xing et al. 2023), have $[Co/Ni] = -0.77 \pm 0.15$ and $[Co/Ni] = -0.55 \pm 0.08$. Zn abundances of the two stars were not determined, only upper limits, and Co and Ni abundances were based on a 1D LTE analysis. Clearly, 3D non-LTE abundances of Co, Ni, and Zn for the PISNe imprint candidates and the high-α and low-α stars used to determine CC and Ia yields would be of high interest.

6. Summary and conclusions

In this paper, we have extended previous determinations (Nissen & Schuster 2010, 2011) of 1D LTE elemental abundances in high-α and low-α halo stars to include Sc, V, and Co, so that the nucleosynthesis of all iron-peak elements from Sc to Zn can be studied along with the lighter elements C, O, Na, Mg, Si, and Ca.

In order to improve the accuracy of the abundance determinations, new 3D non-LTE corrections for Mg and 1D non-LTE corrections for Na, Si, Ca, Mn, and Cu were applied. For C and O, 3D non-LTE abundances from Amarsi et al. (2019) were used, and for Ti, Cr, and Fe, we used spectral lines from the ionised species, for which non-LTE corrections of the derived abundances are negligible.

After having applied the 3D non-LTE corrections for the Mg abundances, substructure in the [Fe/Mg]–[Mg/H] diagram of the low-α halo stars emerged (see Fig. 5). A group of six stars with [Mg/H] ~ -0.8 have higher values of [Fe/Mg] than a group of seven stars with similar metallicity. A similar splitting is seen for [Cr/Mg] and [Fe/Na]. Furthermore, there is a striking difference in the kinematics of the two groups suggesting that stars in the high-[Fe/Mg] group have been accreted from the GSE dwarf galaxy and stars in the low-[Fe/Mg] group from the Thamnos galaxy.

The [X/Mg] versus [Mg/H] trends for high-α and low-α halo stars (Fig. 4) were used to study the nucleosynthesis of the elements. By fitting straight lines to the two populations (excluding Thamnos stars from the low-α population), we determined empirical $[X/Fe]_{CC}$ yields from the high-α trends and then $[X/Fe]_{Ia}$ yields from the difference in the trends of the low-α and high-α populations assuming that Mg is a pure CC element. C, O, Na, and Cu have negligible contributions from Ia SNe, whereas Cr, Mn, and Fe have the largest contribution (see the F_X values in Table 3). This agrees with recent results for surviving dSph galaxies (Hill et al. 2019; Kirby et al. 2019).

The estimated uncertainties of the empirical yields range from ±0.06 to ±0.18 dex of which the main part arises from possible systematic errors in the stellar abundances relative to the solar abundances and from the lack of 3D and non-LTE corrections for some of the elements. For elements having such corrections, the effect on the derived [X/Fe] yields ranges from 0.00 dex for Si to +0.08 dex for Mn. We conclude that it would be important to perform 3D non-LTE calculations for other elements (Sc, V, Co, Ni, and Zn in particular) and also to update the corrections for Mn based on full 3D non-LTE calculations.

Predictions of yields from spherical models of CC SNe by Kobayashi et al. (2006, 2020) and Limongi & Chieffi (2018) do not agree well with the empirical $[X/Fe]_{CC}$ yields; the reduced chi-square of the comparison is $\chi^2_r > 8$ (see Fig. 6). Hopefully, the empirical yields can help to constrain free parameters of such models, for example the mass limit for formation of remnants (black wholes or neutron stars). As discussed by Kobayashi et al. (2020), it may, however, be necessary to consider multidimensional models, for example the 2D models with jets by Maeda & Nomoto (2003) and Tominaga (2009), to explain the empirical CC yields of Ti, V, and Co.

The predicted yields for near-M_{Ch} models of Ia SNe by Leung & Nomoto (2018) and Seitenzahl et al. (2013) give a poor fit to the empirical $[X/Fe]_{Ia}$ values, i.e. $\chi^2_r > 12$ (see Fig. 7). These models predict too high [Mn/Fe] and [Ni/Fe] as well as too low [Ca/Fe] and [Ti/Fe] values. Double detonation sub-M_{Ch} models by Gronow et al. (2021) prowide, however, an excellent fit ($\chi^2_r \sim 1.6$) for the right choice of the masses of the C-O core and the He shell. This suggests that sub-M_{Ch} Ia SNe play a dominant role in the chemical evolution of the GSE dwarf galaxy. The same conclusion was reached by Sanders et al. (2021) based on Mn and Ni abundances in the GSE stars. Our conclusion is based on empirical [X/Fe] yields for nine elements of which Ca, Ti, Mn, and Ni are the most important in favour of sub-M_{Ch} models.

Finally, we note that precise knowledge of yields of CC and Ia SNe is important when searching for signatures of massive Pair Instability Supernovae. In particular, it seems that low [Co/Ni] and [Zn/Ni] ratios can be used to identify imprint of PISNe on the abundances of metal-poor stars.

Acknowledgements. We thank the referee for important comments and Chiaki Kobayashi for providing integrated yields for the CC models in Kobayashi et al. (2020). A.M.A. acknowledges support from the Swedish Research Council (VR 2020-03940). Á.S. has received funding from the European Research Council (ERC) under the European Union's Horizon 2020 research and innovation programme (grant agreement No. 804240). W.J.S. wishes to thank Edilberto Sanchez Moreno of the Computing Center for considerable assistance. This research was supported by computational resources provided by the Australian Government through the National Computational Infrastructure (NCI) under the National Computational Merit Allocation Scheme and the ANU Merit Allocation Scheme (project y89). This research has made use of data from the European Space Agency (ESA) mission *Gaia* (`https://www.cosmos.esa.int/gaia`), processed by the *Gaia* Data Processing and Analysis Consortium (DPAC, `https://www.cosmos.esa.int/web/gaia/dpac/consortium`). Funding for the DPAC has been provided by national institutions, in particular the institutions participating in the *Gaia* Multilateral Agreement. This research has made use of the SIMBAD database operated at CDS, Strasbourg, France (Wenger et al. 2000).

References

Amarsi, A. M., & Asplund, M. 2017, MNRAS, 464, 264
Amarsi, A. M., Barklem, P. S., Asplund, M., Collet, R., & Zatsarinny, O. 2018, A&A, 616, A89
Amarsi, A. M., Nissen, P. E., & Skúladóttir, Á. 2019, A&A, 630, A104
Amarsi, A. M., Lind, K., Osorio, Y., et al. 2020, A&A, 642, A62
Amarsi, A. M., Liljegren, S., & Nissen, P. E. 2022, A&A, 668, A68
Aoki, W., Tominaga, N., Beers, T. C., Honda, S., & Lee, Y. S. 2014, Science, 345, 912
Asplund, M., Amarsi, A. M., & Grevesse, N. 2021, A&A, 653, A141
Barklem, P. S. 2016, A&ARv, 24, 9
Barklem, P. S., Amarsi, A. M., Grumer, J., et al. 2021, ApJ, 908, 245
Belokurov, V., & Kravtsov, A. 2022, MNRAS, 514, 689
Belokurov, V., Erkal, D., Evans, N. W., Koposov, S. E., & Deason, A. J. 2018, MNRAS, 478, 611
Belokurov, V., Sanders, J. L., Fattahi, A., et al. 2020, MNRAS, 494, 3880
Bergemann, M. 2011, MNRAS, 413, 2184
Bergemann, M., & Cescutti, G. 2010, A&A, 522, A9
Bergemann, M., Gallagher, A. J., Eitner, P., et al. 2019, A&A, 631, A80
Buder, S., Lind, K., Ness, M. K., et al. 2022, MNRAS, 510, 2407
Casagrande, L., Ramírez, I., Meléndez, J., Bessell, M., & Asplund, M. 2010, A&A, 512, A54
Cescutti, G., & Kobayashi, C. 2017, A&A, 607, A23
de Bennassuti, M., Salvadori, S., Schneider, R., Valiante, R., & Omukai, K. 2017, MNRAS, 465, 926
Decressin, T., Charbonnel, C., & Meynet, G. 2007, A&A, 475, 859
de los Reyes, M. A. C., Kirby, E. N., Seitenzahl, I. R., & Shen, K. J. 2020, ApJ, 891, 85
Donlon, T., & Newberg, H. J. 2023, ApJ, 944, 169
Eitner, P., Bergemann, M., Hansen, C. J., et al. 2020, A&A, 635, A38
Feltzing, S., & Feuillet, D. 2023, ApJ, 953, 143
Fernandes, L., Mason, A. C., Horta, D., et al. 2023, MNRAS, 519, 3611
Fernández-Alvar, E., Carigi, L., Schuster, W. J., et al. 2018, ApJ, 852, 50
Feuillet, D. K., Bovy, J., Holtzman, J., et al. 2018, MNRAS, 477, 2326
Feuillet, D. K., Sahlholdt, C. L., Feltzing, S., & Casagrande, L. 2021, MNRAS, 508, 1489
Fishlock, C. K., Yong, D., Karakas, A. I., et al. 2017, MNRAS, 466, 4672
Ge, Z. S., Bi, S. L., Chen, Y. Q., et al. 2016, ApJ, 833, 161
Gronow, S., Côté, B., Lach, F., et al. 2021, A&A, 656, A94
Gustafsson, B., Edvardsson, B., Eriksson, K., et al. 2008, A&A, 486, 951
Hawkins, K., Jofré, P., Gilmore, G., & Masseron, T. 2014, MNRAS, 445, 2575
Hawkins, K., Jofré, P., Masseron, T., & Gilmore, G. 2015, MNRAS, 453, 758

Hayes, C. R., Majewski, S. R., Shetrone, M., et al. 2018, ApJ, 852, 49
Heger, A., & Woosley, S. E. 2002, ApJ, 567, 532
Helmi, A. 2020, ARA&A, 58, 205
Helmi, A., Babusiaux, C., Koppelman, H. H., et al. 2018, Nature, 563, 85
Hill, V., Skúladóttir, Á., Tolstoy, E., et al. 2019, A&A, 626, A15
Horta, D., Schiavon, R. P., Mackereth, J. T., et al. 2023, MNRAS, 520, 5671
Kaulakys, B. 1991, J. Phys. B At. Mol. Phys., 24, L127
Kirby, E. N., Xie, J. L., Guo, R., et al. 2019, ApJ, 881, 45
Kobayashi, C., Umeda, H., Nomoto, K., Tominaga, N., & Ohkubo, T. 2006, ApJ, 653, 1145
Kobayashi, C., Karakas, A. I., & Lugaro, M. 2020, ApJ, 900, 179
Koppelman, H. H., Helmi, A., Massari, D., Price-Whelan, A. M., & Starkenburg, T. K. 2019, A&A, 631, L9
Kroupa, P. 2008, in Pathways Through an Eclectic Universe, eds. J. H. Knapen, T. J. Mahoney, & A. Vazdekis, ASP Conf. Ser., 390, 3
Lawler, J. E., Wood, M. P., Den Hartog, E. A., et al. 2014, ApJS, 215, 20
Lawler, J. E., Sneden, C., & Cowan, J. J. 2015, ApJS, 220, 13
Lawler, J. E., Hala, Sneden, C., et al. 2019, ApJS, 241, 21
Leenaarts, J., & Carlsson, M. 2009, in The Second Hinode Science Meeting: Beyond Discovery-Toward Understanding, eds. B. Lites, M. Cheung, T. Magara, J. Mariska, & K. Reeves, ASP Conf. Ser., 415, 87
Leung, S.-C., & Nomoto, K. 2018, ApJ, 861, 143
Limberg, G., Souza, S. O., Pérez-Villegas, A., et al. 2022, ApJ, 935, 109
Limongi, M., & Chieffi, A. 2018, ApJS, 237, 13
Lind, K., & Amarsi, A. M. 2024, ARA&A, submitted [arXiv:2401.00697v1]
Lind, K., Asplund, M., Barklem, P. S., & Belyaev, A. K. 2011, A&A, 528, A103
Lind, K., Bergemann, M., & Asplund, M. 2012, MNRAS, 427, 50
Maeda, K., & Nomoto, K. 2003, ApJ, 598, 1163
Magic, Z., Collet, R., Asplund, M., et al. 2013, A&A, 557, A26
Mashonkina, L. I., & Romanovskaya, A. M. 2022, Astron. Lett., 48, 455
Mason, B. D., Wycoff, G. L., Hartkopf, W. I., Douglass, G. G., & Worley, C. E. 2020, VizieR Online Data Catalog: B/wds
Massari, D., Koppelman, H. H., & Helmi, A. 2019, A&A, 630, L4
Matsuno, T., Dodd, E., Koppelman, H. H., et al. 2022a, A&A, 665, A46
Matsuno, T., Koppelman, H. H., Helmi, A., et al. 2022b, A&A, 661, A103
McMillan, P. J. 2017, MNRAS, 465, 76
Myeong, G. C., Vasiliev, E., Iorio, G., Evans, N. W., & Belokurov, V. 2019, MNRAS, 488, 1235
Myeong, G. C., Belokurov, V., Aguado, D. S., et al. 2022, ApJ, 938, 21
Nissen, P. E., & Schuster, W. J. 2010, A&A, 511, L10
Nissen, P. E., & Schuster, W. J. 2011, A&A, 530, A15
Nissen, P. E., Chen, Y. Q., Carigi, L., Schuster, W. J., & Zhao, G. 2014, A&A, 568, A25
Nissen, P. E., Silva-Cabrera, J. S., & Schuster, W. J. 2021, A&A, 651, A57
North, P., Cescutti, G., Jablonka, P., et al. 2012, A&A, 541, A45
Prochaska, J. X., Naumov, S. O., Carney, B. W., McWilliam, A., & Wolfe, A. M. 2000, AJ, 120, 2513
Ramírez, I., Meléndez, J., & Chanamé, J. 2012, ApJ, 757, 164
Salpeter, E. E. 1955, ApJ, 121, 161
Salvadori, S., Bonifacio, P., Caffau, E., et al. 2019, MNRAS, 487, 4261
Sanders, J. L., Belokurov, V., & Man, K. T. F. 2021, MNRAS, 506, 4321
Schuster, W. J., Moitinho, A., Márquez, A., Parrao, L., & Covarrubias, E. 2006, A&A, 445, 939
Schuster, W. J., Moreno, E., Nissen, P. E., & Pichardo, B. 2012, A&A, 538, A21
Seitenzahl, I. R., Ciaraldi-Schoolmann, F., Röpke, F. K., et al. 2013, MNRAS, 429, 1156
Skúladóttir, Á., Salvadori, S., Amarsi, A. M., et al. 2021, ApJ, 915, L30
Tominaga, N. 2009, ApJ, 690, 526
Umeda, H., & Nomoto, K. 2002, ApJ, 565, 385
Ventura, P., D'Antona, F., Mazzitelli, I., & Gratton, R. 2001, ApJ, 550, L65
Vincenzo, F., Spitoni, E., Calura, F., et al. 2019, MNRAS, 487, L47
Weinberg, D. H., Andrews, B. H., & Freudenburg, J. 2017, ApJ, 837, 183
Weinberg, D. H., Holtzman, J. A., Hasselquist, S., et al. 2019, ApJ, 874, 102
Weinberg, D. H., Holtzman, J. A., Johnson, J. A., et al. 2022, ApJS, 260, 32
Wenger, M., Ochsenbein, F., Egret, D., et al. 2000, A&AS, 143, 9
Xiang, M., & Rix, H.-W. 2022, Nature, 603, 599
Xing, Q.-F., Zhao, G., Liu, Z.-W., et al. 2023, Nature, 618, 712
Yan, H. L., Shi, J. R., Nissen, P. E., & Zhao, G. 2016, A&A, 585, A102
Zhao, G., Zhao, Y.-H., Chu, Y.-Q., Jing, Y.-P., & Deng, L.-C. 2012, Res. Astron. Astrophys., 12, 723